The Astrophysical Journal Supplement Series, 207:23 (12pp), 2013 August doi:10.1088/0067-0049/207/2/23

RELATIVISTIC GLOBAL SOLUTIONS OF NEUTRINO-DOMINATED ACCRETION FLOWS

Li Xue[1,2], Tong Liu[1,3], Wei-Min Gu[1], and Ju-Fu Lu[1]
[1] Department of Astronomy and Institute of Theoretical Physics and Astrophysics, Xiamen University, Xiamen, Fujian 361005, China; tongliu@xmu.edu.cn
[2] Nicolaus Copernicus Astronomical Center, Bartycka 18, 00-716 Warszawa, Poland
[3] State Key Laboratory of Theoretical Physics, Institute of Theoretical Physics, Chinese Academy of Sciences, Beijing 100190, China
Received 2013 January 7; accepted 2013 June 3; published 2013 July 18

ABSTRACT

Neutrino-dominated accretion flows (NDAFs) around rotating stellar-mass black holes are plausible candidates for the central engines of gamma-ray bursts (GRBs). We investigate one-dimensional global solutions of NDAFs, taking into account general relativity in the Kerr metric, neutrino physics, and nucleosynthesis more precisely than previous works. We calculate 16 solutions with different characterized accretion rates and black hole spins to exhibit the radial distributions of various physical properties in NDAFs. We confirm that the electron degeneracy has important effects in NDAFs and we find that the electron fraction is about 0.46 in the outer region for all 16 solutions. From the perspective of the mass fraction, free nucleons, ^{4}He, and ^{56}Fe dominate in the inner, middle, and outer regions, respectively. The influence of neutrino trapping on the annihilation is of importance for the superhigh accretion ($\dot{M} = 10\,M_\odot\,\mathrm{s}^{-1}$) and most of the 16 solutions have an adequate annihilation luminosity for GRBs.

Key words: accretion, accretion disks – black hole physics – gamma-ray burst: general – nuclear reactions, nucleosynthesis, abundances

Online-only material: color figures

1. INTRODUCTION

The observations of gamma-ray bursts (GRBs) are well explained by the relativistic fireball shock model to some extent. However, the central engine powering the fireball is always hidden inside due to the extremely thick optical depth of the fireball. A popular model of the central engine, neutrino-dominated accretion flows (NDAFs), involves a hyperaccreting stellar-mass black hole with accretion rates in the range of 0.01–10 $M_\odot\,\mathrm{s}^{-1}$. This model has been widely applied to explain the variable light curves, extended emission, X-ray flares, associated supernovae, gravitational radiation, and others in GRBs in the past decade (e.g., Popham et al. 1999; Narayan et al. 2001; Di Matteo et al. 2002; Kohri & Mineshige 2002; Kohri et al. 2005; Lee et al. 2005; Gu et al. 2006; Chen & Beloborodov 2007; Janiuk et al. 2007; Kawanaka & Mineshige 2007; Liu et al. 2007, 2008, 2010a, 2010b, 2012a, 2012b, 2013; Lei et al. 2009; Romero et al. 2010; Sun et al. 2012; Kawanaka & Kohri 2012; Li & Liu 2013). In this developing route of NDAF theory, much more detailed and precise microphysics has been widely introduced to improve the theory (see, e.g., Kato et al. 2008).

The relativistic global solutions of NDAFs were first worked out by Popham et al. (1999). They found that the inner region of NDAFs is in an extremely hot and dense state and the free electrons are in a degenerated state in which the photons are totally trapped and only neutrinos can escape to carry away the viscously dissipated gravitational energy. Those neutrinos collide with each other and neutrino pairs annihilate in a funnel space above the inner disk of NDAFs to produce a relativistic fireball of a GRB event. In their solutions, they assumed that NDAFs are always optically thin everywhere for neutrinos, even for the case with extremely high accretion rate, and they oversimplified the treatment of neutrino production and electron degeneracy. These result in an overstated annihilation luminosity, especially for high accretion rate, and lose a lot of microphysics information. Therefore, many subsequent research works have been dedicated to improving the microphysics of NDAFs (e.g., Di Matteo et al. 2002; Kohri & Mineshige 2002; Kohri et al. 2005; Lee et al. 2005; Janiuk et al. 2007). Some elaborate physical considerations, such as defining the neutrino optical depth, precise treatment of electron degeneracy, and electron fraction, were introduced to improve the NDAF theory step by step. Gu et al. (2006) showed that general relativistic effects should be considered and that the contribution from the region optically thick to neutrinos should also be included. Under such consideration, they found that NDAFs can still work as the central engine of the GRB from the viewpoint of energy. Liu et al. (2007) studied the radial structure and neutrino annihilation luminosity of NDAFs. They introduced a bridging formula to treat the radial distribution of the electron fraction between neutrino optically thin and thick limits, but they ignored the existence of heavy-metal elements and assumed that the heaviest nucleus is ^{4}He, which implies that the numerical value of the electron fraction at the radial outer boundary is 0.5. Chen & Beloborodov (2007) presented calculations of the structure of NDAFs around Kerr black holes and proved that both the electron degeneracy and the electron fraction dramatically affect the structure. They also considered that ^{4}He abounded in the outer region of the disk. The ignition radius and other characteristic radii are defined in their work. Kawanaka & Mineshige (2007) investigated NDAFs around Schwarzschild black hole with pseudo-Newtonian potential (Paczyński & Wiita 1980). They assumed that the inflowing nucleon gas is composed primarily of nuclei of a neutron-rich iron group and that the electron fraction is 0.42 at the outer boundary. They studied the radial structure and stability of the disk for different mass accretion rates, using a realistic equation of state (Lattimer & Swesty 1991), in order to properly treat the dissociation of nuclei. Kawanaka & Kohri (2012) studied the effects of convection in NDAFs. They proposed that this process can be used to explain the origin of the highly variable light curves in the prompt emissions of GRBs. Liu et al. (2013) investigated the vertical structure and element

distribution of NDAFs in spherical coordinates with reasonable nuclear statistical equilibrium (NSE; Seitenzahl et al. 2008). According to their calculations, heavy nuclei tend to be produced in a thin region near the disk surface, whose mass fractions are primarily determined by the accretion rate and the vertical distribution of temperature and density. In this thin region, they found that ^{56}Ni is dominant for flow with low accretion rate (e.g., 0.05 $M_\odot$ s^{-1}) but ^{56}Fe is dominant for the high accretion rate counterpart (e.g., 1 $M_\odot$ s^{-1}). The dominant ^{56}Ni in the special region may provide a clue to understand the bumps in the optical light curve of core-collapse supernovae.

In this paper, we return to investigate the relativistic global solutions of NDAF in the Kerr metric, but we fully upgrade the microphysical treatment with detailed neutrino physics and precise NSE based on the improvement of the NDAF theory in the past decade. In Section 2, we establish our physical model for NDAF by introducing the fundamental hydrodynamic and thermodynamic equations, the detailed neutrino processes, and the proton-rich NSE (Seitenzahl et al. 2008; Liu et al. 2013). In Section 3, we describe in detail the numerical methods for the calculations. In Section 4, we show some typical solutions and discuss the results they reveal. We investigate the solutions with different characterized accretion rates and black hole spins. For each case, we calculate the neutrino luminosity and neutrino annihilation luminosity, and show their dependence on these parameters. Conclusions and discussion are made in Section 5.

2. PHYSICAL MODEL

2.1. Relativistic Hydrodynamics

In this paper, we solve for the disk structure in the Kerr metric, because the inner regions of disks may contribute most of the luminosity and it is affected deeply by the spin of the black hole. Our hydrodynamical model of disks is based on the advection-dominated accretion flow model of Abramowicz et al. (1996), the NDAF model of Popham et al. (1999), and the slim disk model of Sądowski (2009), which are all research works on the one-dimensional global solutions of accretion disks in the Kerr metric. For convenience, we describe our hydrodynamical model in units of $G = c = M = 1$ (where M is the mass of black hole), but we use cgs units when we describe the neutrino physics and thermodynamics, and present our results later.

The continuity equation is

$$\dot{M} = -4\pi\rho H\Delta^{1/2}\frac{V_r}{\sqrt{1-V_r{}^2}}, \tag{1}$$

where $\dot{M}$ is the rest-mass accretion rate, ρ is the rest-mass density, H is the half-thickness of disk, V_r is the radial velocity measured in the corotating frame, $\Delta \equiv r^2 - 2r + a^2$ is a function of the Boyer–Lindquist radial coordinate r, and a is the total specific angular momentum of the black hole.

The gas energy equation is

$$-\frac{\dot{M}}{2\pi r^2}\left(\frac{u}{\rho}\frac{d\ln u}{d\ln r} - \frac{p}{\rho}\frac{d\ln\rho}{d\ln r}\right) = -\frac{2\alpha pHA\gamma^2}{r^3}\frac{d\Omega}{dr} - Q^-, \tag{2}$$

where u is the specific internal energy, p is the pressure, α is the viscosity parameter, $A \equiv r^4 + r^2a^2 + 2ra^2$, γ is the Lorentz factor, $\Omega \equiv u^\phi/u^t$ is the angular velocity with respect to the stationary observer, and Q^- is the total cooling rate as described in Section 2.4.

The radial momentum equation is

$$\frac{V_r}{1-V_r{}^2}\frac{dV_r}{dr} = \frac{\mathcal{A}}{r} - (1-V_r{}^2)\frac{1}{\lambda\rho}\frac{dp}{dr}, \tag{3}$$

where

$$\mathcal{A} \equiv -\frac{A}{r^3\Delta\Omega_K^+\Omega_K^-}\frac{(\Omega-\Omega_K^+)(\Omega-\Omega_K^-)}{1-\tilde{\Omega}^2\tilde{R}^2}. \tag{4}$$

The $\mathcal{A}$ term combines the effects of gravity and rotation, where $\lambda \equiv (\rho + p + u)/\rho$ is the relativistic enthalpy, $\tilde{\Omega} \equiv \Omega - 2ar/A$ is the angular velocity with respect to the local inertial observer, $\Omega_K^\pm \equiv \pm(r^{3/2} \pm a)^{-1}$ are the angular frequencies of the corotating and counterrotating Keplerian orbits, and $\tilde{R} \equiv A/(r^2\Delta^{1/2})$ is the radius of gyration.

The equation of angular momentum conservation is

$$\dot{M}(\mathcal{L} - \mathcal{L}_{\rm in}) = \frac{4\pi pHA^{1/2}\Delta^{1/2}\gamma}{r}, \tag{5}$$

where $\mathcal{L} \equiv u_\phi$ is the specific angular momentum of the accreting gas and $\mathcal{L}_{\rm in}$ is the specific angular momentum at the inner edge of the disk.

The equation of vertical mechanical equilibrium (Abramowicz et al. 1997) is

$$\frac{p}{\lambda\rho H^2} = \frac{\mathcal{L}^2 - a^2(\epsilon^2-1)}{r^4}, \tag{6}$$

where $\epsilon \equiv u_t$ is the energy at infinity, which is conserved along geodesics. In a practical calculation, the detailed evaluating formulae of ϵ and γ are necessary,

$$\epsilon = -\gamma\frac{r\Delta^{1/2}}{A^{1/2}} - \frac{2ar}{A}\mathcal{L}, \tag{7}$$

and

$$\gamma = \sqrt{\frac{1}{1-V_r{}^2} + \frac{\mathcal{L}^2r^2}{A}}. \tag{8}$$

2.2. Neutrino Physics

The main difference between NDAF and a typical accretion disk is the cooling mechanism. Neutrino radiation becomes dominant in NDAF, so the microphysics, especially the neutrino physics, must be included in the calculations.

2.2.1. Neutrino Optical Depth

The total optical depth for neutrinos is

$$\tau_{\nu_i} = \tau_{s,\nu_i} + \tau_{a,\nu_i}, \tag{9}$$

where τ_{s,ν_i} and τ_{a,ν_i} are the neutrino optical depth from scattering and absorption, and the subscript i is for the three species of neutrinos ν_e, ν_μ, and ν_τ.

The optical depth for neutrinos through scattering off electrons and nucleons τ_{s,ν_i} is given by

$$\tau_{s,\nu_i} \approx H\left(\sigma_{e,\nu_i}n_e + \sum_j \sigma_{j,\nu_i}n_j\right), \tag{10}$$

where H is the half-thickness of the disk, and σ_{e,ν_i}, σ_{j,ν_i} and n_e, and n_j ($j = 1, 2, ...$) are the cross sections of electrons and nucleons (n_1 and n_2 are the number density of free protons and free neutrons) and the number density of electrons and nucleons ($j \geqslant 3$), respectively (e.g., Kohri et al. 2005; Chen & Beloborodov 2007; Kawanaka & Mineshige 2007; Liu et al. 2007, 2012a). The major cross sections are from scattering off electrons, free protons, free neutrons, and other elements' particles, which are given by (Burrows & Thompson 2004; Chen & Beloborodov 2007)

$$\sigma_{e,\nu_i} \approx \frac{3k_{\rm B}T\sigma_0 e_{\nu_i}}{8m_e c^2}\left(1+\frac{\eta_e}{4}\right)\left[(C_{V,\nu_i}+C_{A,\nu_i})^2 + \frac{1}{3}(C_{V,\nu_i}-C_{A,\nu_i})^2\right], \quad (11)$$

$$\sigma_{n_1,\nu_i} \approx \frac{\sigma_0 e_{\nu_i}^2}{4}[(C_{V,\nu_i}-1)^2+3g_A^2(C_{A,\nu_i}-1)^2], \quad (12)$$

$$\sigma_{n_2,\nu_i} \approx \frac{\sigma_0 e_{\nu_i}^2}{4}\frac{1+3g_A^2}{4}, \quad (13)$$

$$\sigma_{n_j,\nu_i} \approx \frac{\sigma_0}{16}e_{\nu_i}^2(Z_j+N_j)\left[1-\frac{2Z_j}{Z_j+N_j}(1-2\sin^2\theta_W)\right]^2, \quad (14)$$

where $k_{\rm B}$ and η_e are the Boltzmann constant and electron degeneracy, $\sigma_0 = 4G_F^2(m_e c^2)^2/\pi(\hbar c)^4 \approx 1.71\times10^{-44}\,{\rm cm}^2$, $G_F \approx 1.436\times10^{-49}\,{\rm erg\,cm}^3$, e_{ν_i} is the mean energy of neutrinos in units of $(m_e c^2)$, $g_A \approx 1.26$, $\sin^2\theta_W \approx 0.23$, Z_j and N_j are defined as the number of the protons and neutrons of a nucleus X_j, $C_{V,\nu_e} = 1/2+2\sin^2\theta_W$, $C_{V,\nu_\mu} = C_{V,\nu_\tau} = -1/2+2\sin^2\theta_W$, $C_{A,\nu_e} = C_{A,\bar{\nu}_\mu} = C_{A,\bar{\nu}_\tau} = 1/2$, and $C_{A,\bar{\nu}_e} = C_{A,\nu_\mu} = C_{A,\nu_\tau} = -1/2$.

The number density of electrons and positrons is given by the Fermi–Dirac integral (see, e.g., Kohri et al. 2005; Kawanaka & Mineshige 2007; Liu et al. 2007),

$$n_{e^\mp} = \frac{1}{\hbar^3\pi^2}\int_0^\infty dpp^2\frac{1}{e^{(\sqrt{p^2c^2+m_e^2c^4}\mp\mu_e)/k_{\rm B}T}+1}, \quad (15)$$

where $\mu_e = \eta_e k_{\rm B}T$ is the chemical potential of electrons.

The absorption depth for neutrinos τ_{a,ν_i} is given by

$$\tau_{a,\nu_i} = \frac{q_{\nu_i}H}{4(7/8)\sigma T^4}, \quad (16)$$

where q_{ν_i} is the total neutrino cooling rate (per unit volume) and is the sum of four terms,

$$q_{\nu_i} = q_{\rm Urca} + q_{e^-+e^+\to\nu_i+\bar{\nu}_i} + q_{n+n\to n+n+\nu_i+\bar{\nu}_i} + q_{\tilde{\gamma}\to\nu_i+\bar{\nu}_i}. \quad (17)$$

Urca processes have been included in the proton-rich NSE (Seitenzahl et al. 2008; Liu et al. 2013). The neutrino cooling rate due to the Urca processes $q_{\rm Urca}$ relates only to ν_e and, for simplicity, we considered that there are four major terms related to electrons, positrons, free protons, and free neutrons and nucleons (Liu et al. 2007; Kawanaka & Mineshige 2007). In other words, the energy emission rate for electron capture by heavy nuclei is important for the outer region of the disk (Kawanaka & Mineshige 2007). The main energy emission rate is

$$q_{\rm Urca} = q_{p+e^-\to n+\nu_e} + q_{n+e^+\to p+\bar{\nu}_e} + q_{n\to p+e^-+\bar{\nu}_e} + q_{X_j+e^-\to X'_j+\nu_e}, \quad (18)$$

with

$$q_{p+e^-\to n+\nu_e} = \frac{G_F^2\cos^2\theta_c}{2\pi^2\hbar^3c^2}(1+3g_A^2)n_1 \times\int_Q^\infty dE_e E_e\sqrt{E_e^2-m_e^2c^4}(E_e-Q)^3 f_{e^-}, \quad (19)$$

$$q_{n+e^+\to p+\bar{\nu}_e} = \frac{G_F^2\cos^2\theta_c}{2\pi^2\hbar^3c^2}(1+3g_A^2)n_2 \int_{m_ec^2}^\infty dE_e E_e\sqrt{E_e^2-m_e^2c^4}(E_e+Q)^3 f_{e^+}, \quad (20)$$

$$q_{n\to p+e^-+\bar{\nu}_e} = \frac{G_F^2\cos^2\theta_c}{2\pi^2\hbar^3c^2}(1+3g_A^2)n_2 \int_{m_ec^2}^Q dE_e E_e\sqrt{E_e^2-m_e^2c^4}(Q-E_e)^3(1-f_{e^-}), \quad (21)$$

$$q_{X_j+e^-\to X'_j+\nu_e} = \frac{G_F^2\cos^2\theta_c}{2\pi^2\hbar^3c^2}g_A^2\frac{2}{7}N_p(Z_j)N_h(N_j)n_j \int_{Q'}^\infty dE_e E_e\sqrt{E_e^2-m_e^2c^4}(E_e-Q')^3 f_{e^-}, \quad (22)$$

where $\cos^2\theta_c \approx 0.947$, $Q = (m_n-m_p)c^2$, $Q' \approx \mu'_n-\mu'_p+\Delta$, μ'_n and μ'_p are the chemical potential of protons and neutrons in their own nuclei, $\Delta \approx 3$MeV, and $f_{e^\mp} = \{\exp[(E_e\mp\mu_e)/k_{\rm B}T]+1\}^{-1}$ is the Fermi–Dirac function:

$$N_p(Z_j) = \begin{cases} 0, & Z_j < 20, \\ Z_j-20, & 20 < Z_j < 28, \\ 8, & Z_j > 28, \end{cases} \quad (23)$$

$$N_h(N_j) = \begin{cases} 6, & N_j < 34, \\ 40-N_j, & 34 < N_j < 40, \\ 0, & N_j > 40. \end{cases} \quad (24)$$

The third term (also named β decay) is small in comparison with the first two terms, and is usually not included in the literature.

The electron–positron pair annihilation rate into neutrinos $q_{e^-+e^+\to\nu_i+\bar{\nu}_i}$ is (e.g., Itoh et al. 1989; Yakovlev et al. 2001; Janiuk et al. 2007)

$$q_{e^-+e^+\to\nu_i+\bar{\nu}_i} = \frac{Q_c}{36\pi}\left\{\left(C_{V,\nu_i}^2+C_{A,\nu_i}^2\right)^2[8(\Phi_1U_2+\Phi_2U_1)-2(\Phi_{-1}U_2+\Phi_2U_{-1}) + 7(\Phi_0U_1+\Phi_1U_0)]\} + \{[5(\Phi_0U_{-1}+\Phi_{-1}U_0)] + 9\left(C_{V,\nu_i}^2-C_{A,\nu_i}^2\right)^2[\Phi_0(U_1+U_{-1})+(\Phi_{-1}+\Phi_1)U_0]\right\}, \quad (25)$$

where $Q_c = (m_e c/\hbar)^9 G_F^2/\hbar \approx 1.023 \times 10^{23}$ erg cm^{-3} s^{-1}, and the dimensionless functions U_k and Φ_k ($k = -1, 0, 1, 2$) in the above equation can be expressed in terms of the Fermi–Dirac functions (Kawanaka & Mineshige 2007). As we know, when electrons are degenerate, $q_{e^-+e^+\to\nu_i+\overline{\nu}_i}$ becomes negligible.

The nucleon–nucleon bremsstrahlung rate $q_{n+n\to n+n+\nu_i+\overline{\nu}_i}$ is the same for the three species of neutrinos (e.g., Itoh et al. 1996; Di Matteo et al. 2002; Liu et al. 2007),

$$q_{n+n\to n+n+\nu_i+\overline{\nu}_i} \approx 1.5 \times 10^{27} \rho_{10}^2 T_{11}^{5.5} \text{ erg cm}^{-3} \text{ s}^{-1}. \quad (26)$$

We considered the plasmon decay rate $q_{\tilde{\gamma}\to\nu_i+\overline{\nu}_i}$, where plasmons $\tilde{\gamma}$ are photons interacting with electrons (e.g., Kawanaka & Mineshige 2007),

$$q_{\tilde{\gamma}\to\nu_e+\overline{\nu}_e} = \frac{\pi^4}{6\alpha^*} C_{V,\nu_e} \frac{\sigma_0 c}{(m_e c^2)^2} \frac{(k_B T)^9}{(2\pi\hbar c)^6} \gamma^6 \times (\gamma^2 + 2\gamma + 2)\exp(-\gamma), \quad (27)$$

$$q_{\tilde{\gamma}\to\nu_\mu+\overline{\nu}_\mu} = q_{\tilde{\gamma}\to\nu_\tau+\overline{\nu}_\tau} = \frac{4\pi^4}{6\alpha^*} C_{V,\nu_\mu} \frac{\sigma_0 c}{(m_e c^2)^2} \frac{(k_B T)^9}{(2\pi\hbar c)^6} \gamma^6 \times (\gamma^2 + 2\gamma + 2)\exp(-\gamma). \quad (28)$$

$\alpha^* \approx 1/137$ is the fine-structure constant and $\gamma \approx 5.565 \times 10^{-2}[(\pi^2 + 3\eta_e^2)/3]^{1/2}$. Here $q_{n+n\to n+n+\nu_i+\overline{\nu}_i}$ and $q_{\tilde{\gamma}\to\nu_i+\overline{\nu}_i}$ may become important only for very high electron degeneracy states.

2.2.2. Electron Fraction

The electron fraction can be written as (e.g., Liu et al. 2013)

$$Y_e = \frac{\sum_j n_j Z_j}{\sum_j n_j (Z_j + N_j)}. \quad (29)$$

Liu et al. (2007) calculated the electron fraction according to the simple NSE equation, the condition of electrical neutrality, and a bridging formula of electron fraction that is valid in both the optically thin ($\mu_n = \mu_p + 2\mu_e$, where μ_n and μ_p are the chemical potential of free neutrons and protons) and thick ($\mu_n = \mu_p + \mu_e$) regimes. Here we use the strict NSE equations (see Section 2.3) to replace the simple one which assumed that the heaviest nuclei is ^{4}He. Meanwhile, the condition of electrical neutrality still holds, which is given by (Liu et al. 2007, 2013)

$$\sum_j n_j Z_j = \frac{\rho Y_e}{m_u} = n_{e^-} - n_{e^+}, \quad (30)$$

where m_u is the mean mass of the nucleus, and we assumed that the mass fraction approximately equals the number density.

Furthermore, in order to allow for a transition from the optically thin to optically thick regimes, the bridging formula of free protons and neutrons can be established from the relations of the reaction rates in the above β processes, which can be written as (Yuan 2005; Liu et al. 2007)

$$\lg \frac{n_2}{n_1} = f(\tau_\nu) \frac{2\mu_e - Q}{k_B T} + [1 - f(\tau_\nu)] \frac{\mu_e - Q}{k_B T}, \quad (31)$$

where $f(\tau_\nu) = \exp(-\tau_{\nu_e})$ is a weight factor, and μ_e is the chemical potential of electrons. In addition, the bridging formula can also be used even when taking nucleosynthesis into account because the outer region of the disk is optically thin to neutrinos.

2.3. Nucleosynthesis

NSEs established by all nuclear reactions are in chemical equilibrium. Seitenzahl et al. (2008) studied proton-rich material in a state of NSE, which applies to almost the entire range of electron fraction. The complicated and detailed balance has been included under the condition of chemical potential equilibrium. The number density of nuclei j can be considered as

$$n_j = g_j \left(\frac{m_j k_B T}{\hbar^2}\right)^{3/2} \times \exp\left[\frac{Z_j(\mu_p^{\rm kin} + \mu_p^{\rm C}) + N_j \mu_n^{\rm kin} - \mu_j^{\rm C} + Q_j}{k_B T}\right], \quad (32)$$

where $\mu_p^{\rm kin}$ and $\mu_n^{\rm kin}$ are the kinetic chemical potentials of protons and neutrons, $\mu_p^{\rm C}$ and $\mu_j^{\rm C}$ are the Coulomb chemical potentials of protons and nucleons, and g_j are the nuclear partition functions. Seitenzahl et al. showed that ^{56}Ni is favored in NSE under proton-rich conditions ($Y_e \simeq 0.5$) which is different from the case of domination by the Fe-peak nuclei with the largest binding energy per nucleon that has a proton to nucleon ratio close to the prescribed electron fraction. In particular, the lower limit of the temperature in the NSE calculation is identified to be about 2×10^9 K. If the temperature is lower than this limit, the NSE solutions will not be reliable. Therefore, in our calculations we assume that all nuclear reactions would cease when the temperature is lower than this limit.

Thus NSE originates from the study of the proton-rich state of matter, but it can be used in describing all states of matter. The limit of the electron fraction, $Y_e \lesssim 0.5$, has been canceled, and the more real state of matter can be described through these NSE equations. The NSE code in proton-rich environments can be downloaded from http://cococubed.asu.edu/code_pages/nse.shtml.

2.4. Thermodynamics

The contributions to pressure from degenerate electrons and from neutrinos should be included in the equation of state. It can be written as

$$p = p_{\rm gas} + p_{\rm rad} + p_e + p_\nu. \quad (33)$$

The gas pressure from free nucleons $p_{\rm gas}$ is

$$p_{\rm gas} = \sum_j n_j k_B T. \quad (34)$$

The disk is definitely optically thick to photons, so the photon radiation pressure $p_{\rm rad}$ is

$$p_{\rm rad} = aT^4/3. \quad (35)$$

The electron pressure p_e is from both electrons and positrons and should be calculated using the exact Fermi–Dirac distribution (e.g., Chen & Beloborodov 2007; Liu et al. 2007). No asymptotic expansions are valid because electrons are neither nondegenerate nor strongly degenerate, and they are not ultra-relativistic at all radii. It reads

$$p_e = p_{e^-} + p_{e^+}, \quad (36)$$

with

$$p_{e^{\mp}} = \frac{1}{3\pi^2\hbar^3c^3}\int_0^\infty dp \frac{p^4}{\sqrt{p^2c^2+m_e{}^2c^4}} \times \frac{1}{e^{(\sqrt{p^2c^2+m_e{}^2c^4}\mp\mu_e)/k_BT}+1}. \quad (37)$$

Pan & Yuan (2012a, 2012b) calculated the one-dimensional Boltzmann equation of neutrino and anti-neutrino transport in accretion disks. From the solutions of NDAFs, the bridging formula valid in the regimes optically thin and thick to neutrinos can also be used as a good approximation. We adopt the formula for the energy density of neutrinos u_ν (e.g., Di Matteo et al. 2002; Kohri et al. 2005; Liu et al. 2007),

$$u_\nu = \sum_i \frac{(7/8)aT^4(\tau_{\nu_i}/2+1/\sqrt{3})}{\tau_{\nu_i}/2+1/\sqrt{3}+1/(3\tau_{a,\nu_i})}. \quad (38)$$

The neutrino pressure p_ν is

$$p_\nu = \frac{u_\nu}{3}. \quad (39)$$

The cooling rate appearing in Equation (2) is composed of the cooling rates of photodisintegration, neutrino emitting, and photon radiation:

$$Q^- = Q_{\rm ph} + Q_\nu + Q_{\rm rad}. \quad (40)$$

However, the cooling due to photon radiation is always much smaller than the other two and so we ignore $Q_{\rm rad}$ in this paper.

The cooling rate due to photodisintegration $Q_{\rm ph}$, which is mainly related to α particles, can be written as

$$Q_{\rm ph} = 6.8\times10^{28}\rho_{10}V_rH\frac{dX_{\rm nuc}}{dr}\ {\rm cgs\ units}, \quad (41)$$

where $\rho_{10}\equiv\rho/10^{10}\ {\rm g\ cm^{-3}}$ and $X_{\rm nuc}$ is the mass fraction of free nucleons (e.g., Kohri et al. 2005; Liu et al. 2007). Here we ignore the cooling rate due to the disintegration of other heavy nuclei because of the lower number density of these nuclei and the absolutely dominant advective cooling rate in the outer region.

The cooling rate due to neutrino loss Q_ν is expressed in accordance with the above equation of energy density of neutrinos (e.g., Di Matteo et al. 2002; Kohri et al. 2005; Liu et al. 2007),

$$Q_\nu = \sum_i \frac{(7/8)\sigma T^4}{(3/4)[\tau_{\nu_i}/2+1/\sqrt{3}+1/(3\tau_{a,\nu_i})]}. \quad (42)$$

2.5. Neutrino Luminosity and Neutrino Annihilation Luminosity

The neutrino radiation luminosity can be calculated by integrating the neutrino cooling rate Q_ν along the disk, which is obtained to be

$$L_\nu = 4\pi\int_{\max(r_{\rm ms},r_{\rm tr})}^{r_{\rm out}} Q_\nu r dr, \quad (43)$$

where $r_{\rm out}$ is the outer edge of the disk, which is fixed to 500 Schwarzschild radius in our calculations. The lower bound is defined to be the larger of the neutrino trapping radius $r_{\rm tr}$ and the marginally stable radius of the black hole $r_{\rm ms}$, in order to take into account the effect of neutrino trapping.

In classic accretion theory, the radiation energy generated near the equatorial plane diffuses toward the disk surface at the speed of $\sim c/3\tau$ (Mihalas & Weibel Mihalas 1984), where τ is the total optical depth. Thus, the timescale of radiative diffusion is $t_{\rm diff} = H/(c/3\tau)$ (e.g., Ohsuga et al. 2002). We use V_n for neutrinos and c for photons, which is related to the energy of neutrinos $\sim3.7k_BT$ (e.g., Di Matteo et al. 2002; Liu et al. 2007, 2012a). V_n can be estimated as $\sim(3.7k_BTc^2/0.07\ {\rm eV})^{1/2}$, where 0.07 eV roughly equals the low limit of the neutrino rest-mass energy. Since the accretion timescale $t_{\rm acc}$ is given by $-r/V_r$, the condition in which the neutrino radiation energy is trapped in the flow and falls onto black hole is $t_{\rm diff} > t_{\rm acc}$. If only the electron neutrino optical depth is considered, we can approximatively define the trapping radius:

$$r_{\rm tr} \simeq -\frac{3\tau_{\nu_e}HV_r}{V_n}. \quad (44)$$

Obviously, the effect of neutrino trapping will greatly affect the annihilation luminosity.

To calculate the neutrino annihilation luminosity, we follow the approach in Ruffert et al. (1999), Popham et al. (1999), Rosswog et al. (2003), Liu et al. (2007), and Kawanaka et al. (2012). The disk is modeled as a grid of cells in the equatorial plane. A cell k has its mean neutrino energy $\varepsilon^k_{\nu_i}$, neutrino radiation luminosity $l^k_{\nu_i}$, and distance to a space point above (or below) the disk d_k. $l^k_{\nu_i}$ can be calculated using the surface integral of the cooling rate of each flavor of neutrino in cell k according to the form of Equation (42) before summation. The angle at which neutrinos from cell k encounter antineutrinos from another cell k' at that point is denoted as $\theta_{kk'}$. Then the neutrino annihilation luminosity at that point is given by the summation over all pairs of cells,

$$l_{\nu\bar{\nu}} = \sum_i A_{1,i}\sum_k\frac{l^k_{\nu_i}}{d_k^2}\sum_{k'}\frac{l^{k'}_{\bar{\nu}_i}}{d_{k'}^2}\left(\varepsilon^k_{\nu_i}+\varepsilon^{k'}_{\bar{\nu}_i}\right)(1-\cos\theta_{kk'})^2 + \sum_i A_{2,i}\sum_k\frac{l^k_{\nu_i}}{d_k^2}\sum_{k'}\frac{l^{k'}_{\bar{\nu}_i}}{d_{k'}^2}\frac{\varepsilon^k_{\nu_i}+\varepsilon^{k'}_{\bar{\nu}_i}}{\varepsilon^k_{\nu_i}\varepsilon^{k'}_{\bar{\nu}_i}}(1-\cos\theta_{kk'}), \quad (45)$$

where $A_{1,i} = (1/12\pi^2)[\sigma_0/c(m_ec^2)^2][(C_{V,\nu_i}-C_{A,\nu_i})^2 + (C_{V,\nu_i}+C_{A,\nu_i})^2]$, $A_{2,i} = (1/6\pi^2)(\sigma_0/c)\ (2C^2_{V,\nu_i}-C^2_{A,\nu_i})$. The total neutrino annihilation luminosity is obtained by integrating over the whole space outside the black hole and the disk:

$$L_{\nu\bar{\nu}} = 4\pi\int_{\max(r_{\rm ms},r_{\rm tr})}^\infty\int_H^\infty l_{\nu\bar{\nu}}rdrdz, \quad (46)$$

where the inner edge is dependent on the status of neutrino trapping (e.g., Di Matteo et al. 2002; Liu et al. 2012a).

3. NUMERICAL METHODS

To obtain the disk solutions, we have to solve the fundamental equations (1), (2), (3), (5), (6), and (31) for the independent variables ρ, T, V_r, $\mathcal{L}$, H, and μ_e. In this paper, we follow Matsumoto et al. (1984) in using the shooting method for solving these equations, which is one of the popular methods for solving the boundary value problem of differential equations. However, there are two obstacles for solving these equations using the

shooting method. One is the instability of numerical integration and the other is the sonic point.

The first obstacle is due to the stiffness of these equations. It is numerically unstable to integrate the equations inward with a certain explicit method (e.g., Runge–Kutta method). Fortunately, this integration instability can be overcome by implicit integration. In this paper, we follow Matsumoto et al. (1984) in using the first-order backward Euler method in shooting integration. In this method, for example, the differential equation $df/dr = g$ is approximated by the backward difference as $(f_{i+1} - f_i)/(r_{i+1} - r_i) = g_{i+1}$, where g is an algebraic expression of f, and the value of f is known on the grid point r_i but unknown on r_{i+1}. With this kind of approximation, Equations (1), (2), (3), (5), (6), and (31) are reduced to six nonlinear algebraic equations for the independent variables ρ_{i+1}, T_{i+1}, $V_{r,i+1}$, $\mathcal{L}_{i+1}$, H_{i+1}, and $\mu_{e,i+1}$. In each integration step, we solve these equations using to Newton–Raphson method. The initial guesses for the independent variables on r_{i+1} are set to be the determined values on r_i, which are either the results of the last step or the boundary values in the first step. Even though the first-order backward Euler scheme is less accurate than other alternative high-order difference schemes (e.g., the central difference scheme), we found, in practice, that it is a good method for overcoming the stiffness in our equations and has a faster converging speed in integration than other high-order implicit difference schemes.

The other obstacle is due to the sonic point. As mentioned in many previous works (e.g., Sądowski 2009; Matsumoto et al. 1984), the derivative $d \ln V_r / d \ln r$ would tend to a 0/0 form limit when the radial velocity tends to the local sound speed of the accreted gas. In fact, the numerical computations are performed in a computer with a finite machine accuracy, so the sonic point cannot be really reached but only approached and spanned from the subsonic region to the supersonic region. Matsumoto et al. (1984) presented a detailed and completed research on the mathematical and physical properties of the sonic points in viscous transonic flows. Benefiting from their research, we use their adaptive grid scheme to perform the shooting integration (see the details in Appendix 2 of Matsumoto et al. 1984), which showed a robust ability for transonic integration in our work.

After overcoming the above two obstacles, using the shooting integration to solve our equations becomes possible. The angular momentum at the inner edge of the disk, $\mathcal{L}_{\rm in}$, becomes the eigenvalue of the shooting integration. At the beginning of the first shooting, we set the guessed value of $\mathcal{L}_{\rm in}$ to be the Keplerian angular momentum at the marginally stable orbit. If the guessed value is larger than the proper value $\mathcal{L}_{\rm in,0}$, the integration will be unable to converge near the sonic point. However, if the guessed value is less than $\mathcal{L}_{\rm in,0}$, a fully subsonic solution will be obtained. If the former case is met, the failed value will be used to update the upper limit of $\mathcal{L}_{\rm in}$; on the contrary, if the latter case occurs, the lower limit will be updated. After updating the upper and lower limits, a new shooting will begin with a different guessed $\mathcal{L}_{\rm in}$, the value of which is set to be the midpoint of those limits. This kind of shooting integration is repeated until a self-consistent transonic solution is obtained.

4. NUMERICAL RESULTS

In our NDAF model, there are four parameters, the viscous parameter α, black hole mass M, dimensionless black hole spin a_* ($\equiv a/M$), and dimensionless accretion rate $\dot{m}$ [$\equiv \dot{M}/(M_\odot\,{\rm s}^{-1})$]. In order to concentrate on the more important effects of the different black hole spins and accretion rates, we fix the viscous parameter and black hole mass with the typical values of NDAF, $\alpha = 0.1$ and $M = 3\,M_\odot$, and investigate 16 solutions with different black hole spins $a_* = 0, 0.5, 0.9, 0.99$ and accretion rates $\dot{m} = 0.03, 0.1, 1, 10\,M_\odot\,{\rm s}^{-1}$. The selected values of a_* cover the cases with no, moderate, high, and extreme spins of the black holes, which is an essential qualification for the emergence of jet breakout in collapsars, the plausible progenitor of long GRBs (e.g., Nagakura et al. 2011; Nagakura 2012). Meanwhile, the selected values of $\dot{m}$ correspond to the cases with low, moderate, high, and superhigh accretion rates. These solutions can be obtained by numerically solving the fundamental equations (1), (2), (3), (5), (6), and (31) using the numerical method described in Section 3.

4.1. Structure

In Figure 1, we show the structures of the 16 solutions in order to compare them with each other. There are six panels and they correspond to the profiles of density ρ, temperature T, radial velocity V_r, electron degeneracy η_e, optical depth of electron neutrino τ_{ν_e}, and electron fraction Y_e. They reveal different variations: ρ increases by about six orders of magnitude, T increases by about one order of magnitude, and τ_{ν_e} increases by about five orders of magnitude from the outer to the inner region, and, in the innermost region, which is extremely dense, hot, and optically thick to neutrinos (see, e.g., Li & Liu 2013), ρ reaches $\sim 10^{13}\,{\rm g\,cm^{-3}}$, T reaches $\sim 10^{12}\,{\rm K}$, and τ_{ν_e} reaches $\sim$1000. The difference between the effects of the accretion rate and the black hole spin is obvious. One can find that the profiles can be collected into four groups with the same color (i.e., the same accretion rate). It implies that the effect of accretion rate is global. Meanwhile, the profiles with different line styles (different black hole spins) in a colored group become more and more dispersed from to outer to the inner region. It implies that the effect of black hole spin becomes remarkable only close to the black hole.

There is a remarkable feature in the profiles of the radial velocity. They all tend toward the speed of light c in the inner region and the radii satisfy $V_r/c = 1$ (the locations of the black hole horizon), which are only determined by the black hole spin. It proves that our model and the calculations are all consistent with general relativity.

Electron degeneracy is an important physical parameter that affects electron fraction, degeneracy pressure, and neutrino cooling (Chen & Beloborodov 2007). The profiles of η_e, which represents the degree of electron degeneracy, in Figure 1 are similar to the ones of Chen & Beloborodov (2007) and Kawanaka & Mineshige (2007). However, there is a slight difference between the profiles of Y_e in Figure 1 and previous works (e.g., Liu et al. 2007; Chen & Beloborodov 2007; Kawanaka & Mineshige 2007). While our Y_e can become larger than 0.5 because of the different description of NSE we used, they cannot become larger in those previous works. Our Y_e all tend to $\sim$0.46 at the outer boundary of the disk, which have a slightly different value, $\sim$0.42, in Kawanaka & Mineshige (2007).

In Figure 2, we show the contributions to the total pressure p from the gas pressure of nucleons $p_{\rm gas}$, radiation pressure of photons $p_{\rm rad}$, degeneracy pressure of electrons p_e, and radiation pressure of neutrinos p_ν. Similar to what is seen in Figure 1, the effect of black hole spin is revealed by the dispersion of the profiles with different line styles in a colored group. More dispersion implies more remarkable effects. One can see that the

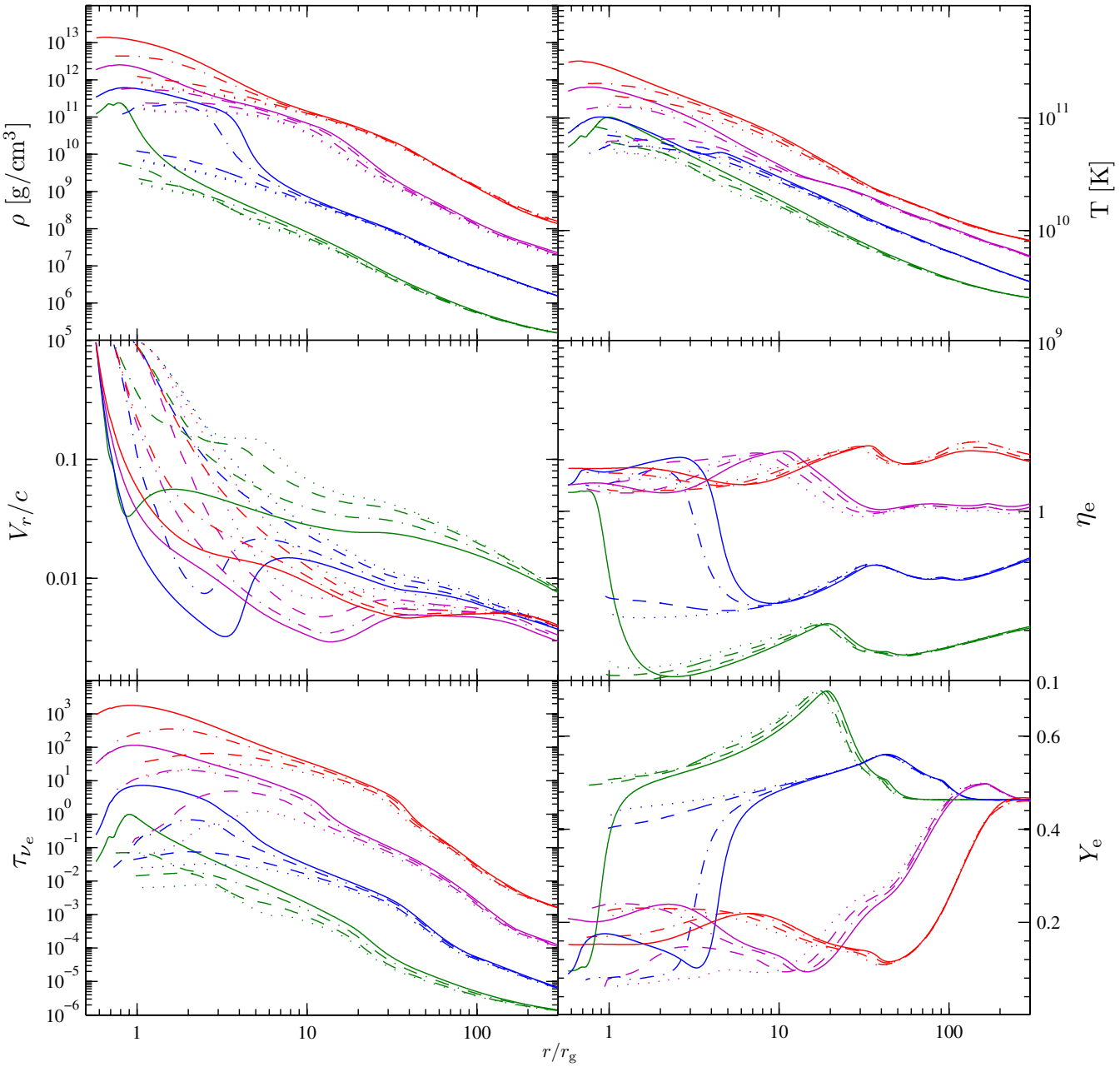

Figure 1. Profiles for the 16 solutions. The colors green, blue, purple, and red denote the different accretion rates $\dot{m} = 0.03$, 0.1, 1, and 10, respectively. The line styles, dotted, dashed, dot-dashed, and solid, denote the different black hole spins $a_* = 0$, 0.5, 0.9, and 0.99, respectively. The six panels show the profiles for density ρ, temperature T, radial velocity V_r, electron degeneracy η_e, optical depth of electron neutrino τ_{ν_e}, and electron fraction Y_e from left to right and from top to bottom, respectively.

(A color version of this figure is available in the online journal.)

effects of black hole spins are still constrained in the inner region as seen in Figure 1. However, a small detail revealed in Figure 2 should be mentioned here. The effects of black hole spins on the solutions with moderate ($\dot{m} = 0.1$) and high ($\dot{m} = 1$) accretion rates are more remarkable (more dispersive) than the solutions with low ($\dot{m} = 0.03$) and superhigh ($\dot{m} = 10$) accretion rates. The reasons are that the cooling due to neutrino radiation in the low accretion case is too weak to be sensitive to black hole spins only, except for the solution with an extreme black hole spin, whereas the effect of black hole spin is damped by the superhigh accretion rate so that it is also insensitive to black hole spins in the case with superhigh accretion rate.

Focusing on the profiles of p_e/p and $p_{\rm gas}/p$ in Figure 2, one can see that the contributions of $p_{\rm gas}$ exceed p_e in some certain radii. This only happens in cases with high or extreme black hole spins in the solutions with low and moderate accretion rates, while they always happen in solutions with high and superhigh accretion rates and their locations shift outward for larger accretion rates. These are also due to the competition between the effects of black hole spin and accretion rate on neutrino cooling.

For the contributions of the radiation pressure of neutrinos p_ν, one can see that they are fully ignorable in the outer region, which is always optically thin to neutrinos, while they become notable and even exceed the photon radiation pressure in the inner region, which is optically thick to neutrino.

In Figure 3, we show the cooling rates normalized by the viscous heating rate $Q_{\rm vis}$. The photon coolings in our solutions

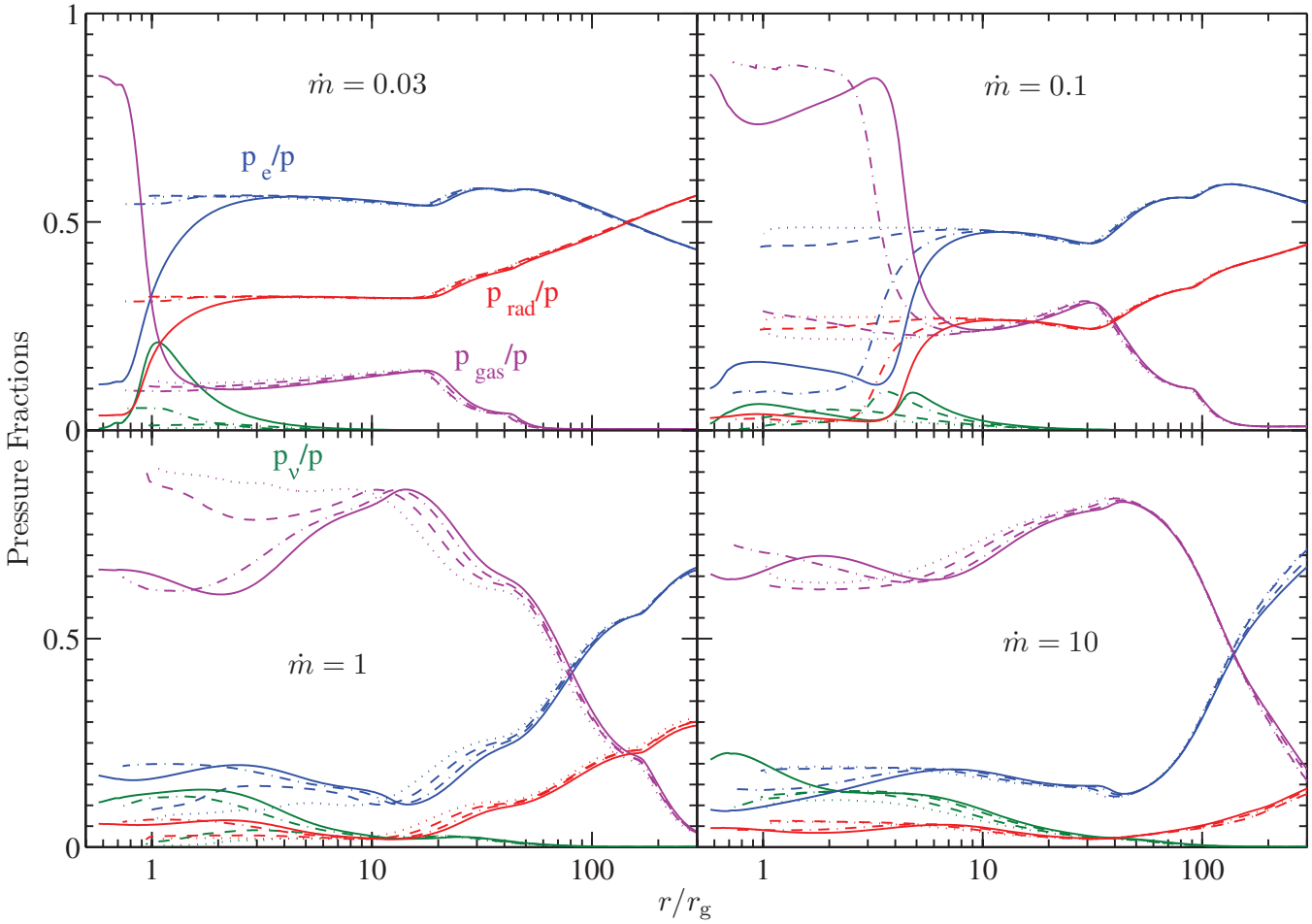

Figure 2. Contributions to the total pressure p. Here, the colors blue, red, purple, and green denote the different contributions from the degeneracy pressure of electrons p_e, radiation pressure of photons $p_{\rm rad}$, gas pressure of nucleons $p_{\rm gas}$, and radiation pressure of neutrinos p_ν, respectively. The meanings of the line styles are the same as in Figure 1. The four panels correspond to the different accretion rates.

(A color version of this figure is available in the online journal.)

are always much lower than the other coolings, so we ignore it in this figure. The profiles of our $Q_{\rm adv}/Q_{\rm vis}$ are very similar to the ones in Popham et al. (1999). $Q_{\rm adv}/Q_{\rm vis} \sim 1$ in the outer region implies that the flow is advection-dominated. Photodisintegration cooling causes the decrease of $Q_{\rm adv}/Q_{\rm vis}$, even becoming negative in the outer and middle regions. Neutrino cooling causes $Q_{\rm adv}/Q_{\rm vis}$ to decrease to negative again in the inner region. All of these behaviors are consistent with the relevant results of previous works (e.g., Popham et al. 1999; Liu et al. 2007; Chen & Beloborodov 2007). The special behavior of $Q_{\rm adv}/Q_{\rm vis}$ and $Q_\nu/Q_{\rm vis}$ wherein their values rapidly increase to much larger than unity near the inner edge of disks is due to the rapid decrease of viscous heating $Q_{\rm vis}$ in the fast inflowing flows.

Since we have considered detailed nucleosynthesis in our model, we can obtain and trace the radial variation of more than 40 nucleons with our calculation. Figure 4 shows the radial distributions of the mass fractions of seven major nucleons, ^1n, ^{1}H, ^{4}He, ^{52}Cr, ^{54}Cr, ^{56}Fe, and ^{58}Fe, which cover almost 99% of the mass of the flow. The mass fraction of ^{56}Fe dominates in the outer region for all accretion rates. In the middle region, ^{4}He dominates for all accretion rates. Free neutrons and protons dominate via photodisintegration in the inner region, which is in the hot and dense state. The size of the region dominated by free nucleons is determined by the accretion rate. The spin of the black hole is also affected by the proportion of free protons and neutrons in the inner region. Most of the free protons turn into free neutrons via the Urca process (e.g., Liu et al. 2007; Kawanaka & Mineshige 2007), which causes the free neutrons to dominate and the electron fraction to decrease. Compared to Chen & Beloborodov (2007) and Liu et al. (2007), wherein heavier nuclei appeared in the outer region of the disk, we have described a more possible structure and component distribution. It implies that heavy nuclei originate in GRBs, which accounts for the detection of Fe Kα X-ray lines and other emission lines (e.g., Lazzati et al. 1999), which can play an important role in understanding the nature of GRBs, especially its central engine. The neutron-rich NSE has been used in Kawanaka & Mineshige (2007; unfortunately, they did not show the distribution of heavy nuclei in the outer disk), wherein the electron fraction Y_e has been limited to less than 0.5. The reasonable NSE we chose requires that the range for Y_e be [0, 1], which can certify that the solutions naturally and reasonably. Compared with Liu et al. (2013), the kinds and distributions of elements are not different in the radial and vertical coordinates. ^{56}Ni dominates at the disk surface for lower accretion rate (e.g., 0.05 $M_\odot$ s^{-1}), and ^{56}Fe dominates for larger accretion rate (e.g., 1 $M_\odot$ s^{-1}), corresponding to Y_e around 0.49 and 0.47, respectively. In addition, according to Equation (29), the profiles of Y_e in Figure 1 can be obtained

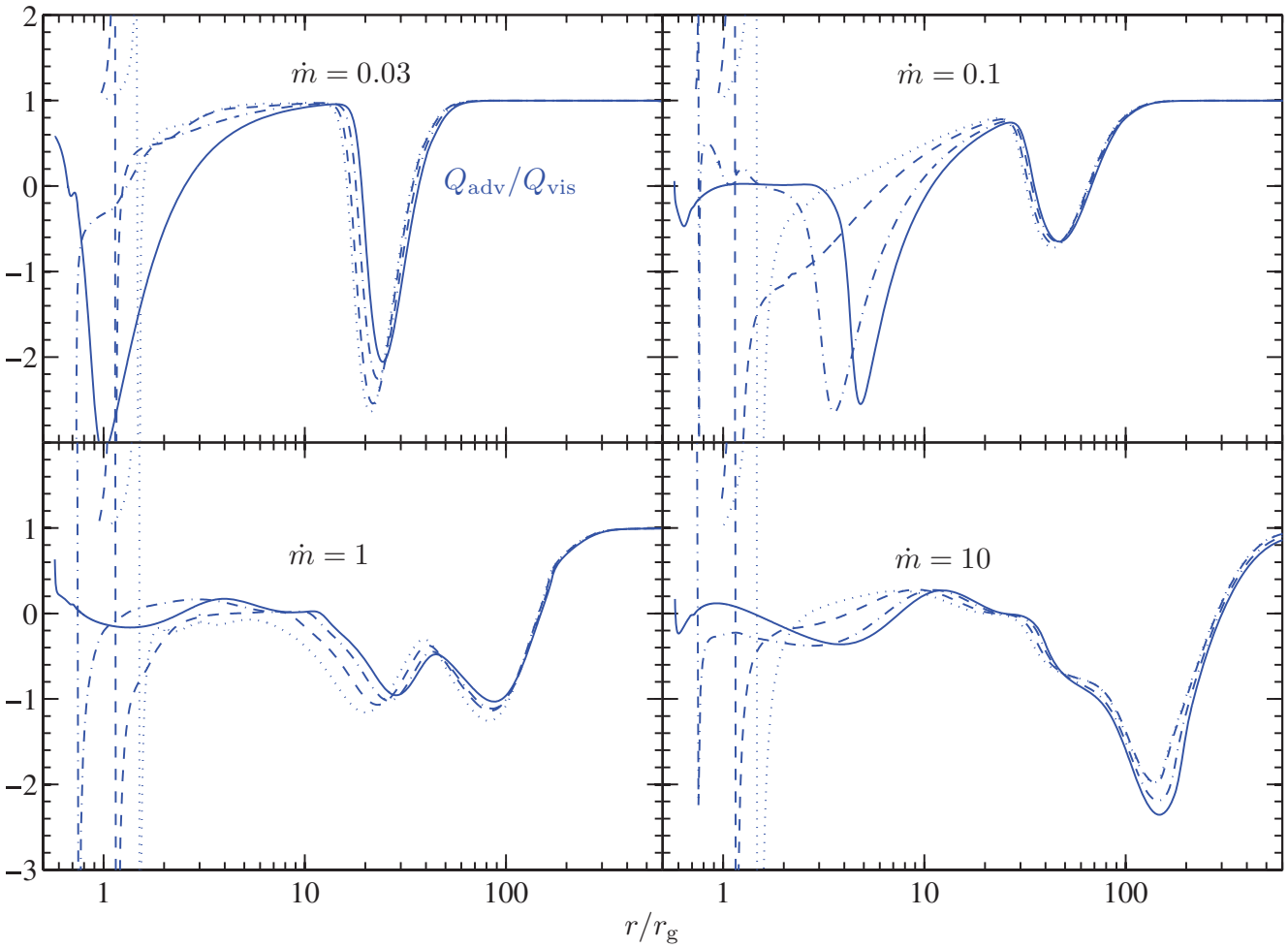

Figure 3. Cooling rates normalized by the viscous heating rate $Q_{\rm vis}$. The upper four panels exhibit the normalized advection cooling rates $Q_{\rm adv}/Q_{\rm vis}$ and the lower four panels are for the normalized neutrino cooling rates $Q_\nu/Q_{\rm vis}$ and photodisintegration cooling rates $Q_{\rm ph}/Q_{\rm vis}$. The meanings of different line styles are same as in Figures 1 and 2.

(A color version of this figure is available in the online journal.)

from Figure 4 if we consider that the mass fraction approximately equals the number density.

4.2. Luminosity

In this paper, we are concerned with the energetic estimation for boosting GRB through neutrino annihilation outside NDAF. Therefore, we are only concerned with the total annihilation luminosity but not the exact distribution of the annihilation energy and we calculate the neutrino trapping radius and the annihilation luminosity without taking into account the general relativistic effects on the neutrino trajectory to avoid complexity in this calculation. In Table 1, we list the neutrino radiation luminosity L_ν, neutrino annihilation luminosity $L_{\nu\bar{\nu}}$, efficiency of energy deposition $L_{\nu\bar{\nu}}/L_\nu$, neutrino trapping radius $r_{\rm tr}$, and the radius of the marginally stable orbit $r_{\rm ms}$ of our 16 solutions. The upper limit of neutrino luminosity reaches about $10^{55}\,{\rm erg\,s^{-1}}$, which is near the limit of the power of the Kerr black hole, for the solution with $\dot{m} = 10$ and $a_* = 0.99$. We note that most of the results on neutrino annihilation luminosity are higher than $10^{49}\,{\rm erg\,s^{-1}}$ and thus are likely to be adequate for GRBs (Zhang 2011) even when taking into account the effect of neutrino trapping, especially for the high accretion rate and rapidly spinning black hole.

Compared with the work of Popham et al. (1999), our $L_{\nu\bar{\nu}}$ is much smaller than theirs for the solutions with superhigh accretion rate ($\dot{m} = 10$) since we consider the effects of neutrino trapping. In particular, they had $L_{\nu\bar{\nu}} = 2\times10^{53}\,{\rm erg\,s^{-1}}$ for $a_* = 0$, $\dot{m} = 10$, and $L_{\nu\bar{\nu}} = 8.2\times10^{53}\,{\rm erg\,s^{-1}}$ for $a_* = 0.5$, $\dot{m} = 10$, while we obtain more reasonable values $L_{\nu\bar{\nu}} = 2.94\times10^{52}\,{\rm erg\,s^{-1}}$ and $L_{\nu\bar{\nu}} = 3.17\times10^{52}\,{\rm erg\,s^{-1}}$, respectively. This implies that the influence of neutrino trapping cannot be ignored especially for the superhigh accretion cases.

Zalamea & Beloborodov (2011) fully considered the general relativistic effects on the neutrino trajectory in their annihilation calculation. They compared their results with Popham et al. (1999). They stated that $L_{\nu\bar{\nu}}$ would be overestimated 10 times by the calculation that does not take general relativistic effects into account. Thus, taking a conservative estimate, the 10 times lower $L_{\nu\bar{\nu}}$ listed in Table 1 can be regarded to be reasonable approximate values. Based on the results in Table 1, we approximate the neutrino radiation luminosity, annihilation luminosity, and neutrino trapping radius with three analytic formulae as functions of black hole spin and accretion rate:

$$\log L_\nu({\rm erg\,s^{-1}}) \approx 52.5 + 1.17a_* + 1.17\log\dot{m}, \quad (47)$$

$$\log L_{\nu\bar{\nu}}({\rm erg\,s^{-1}}) \approx 49.5 + 2.45a_* + 2.17\log\dot{m}, \quad (48)$$

$$r_{\rm tr}/r_g \approx -0.92 + 2.42a_* + 5.95\log\dot{m}, \quad (49)$$

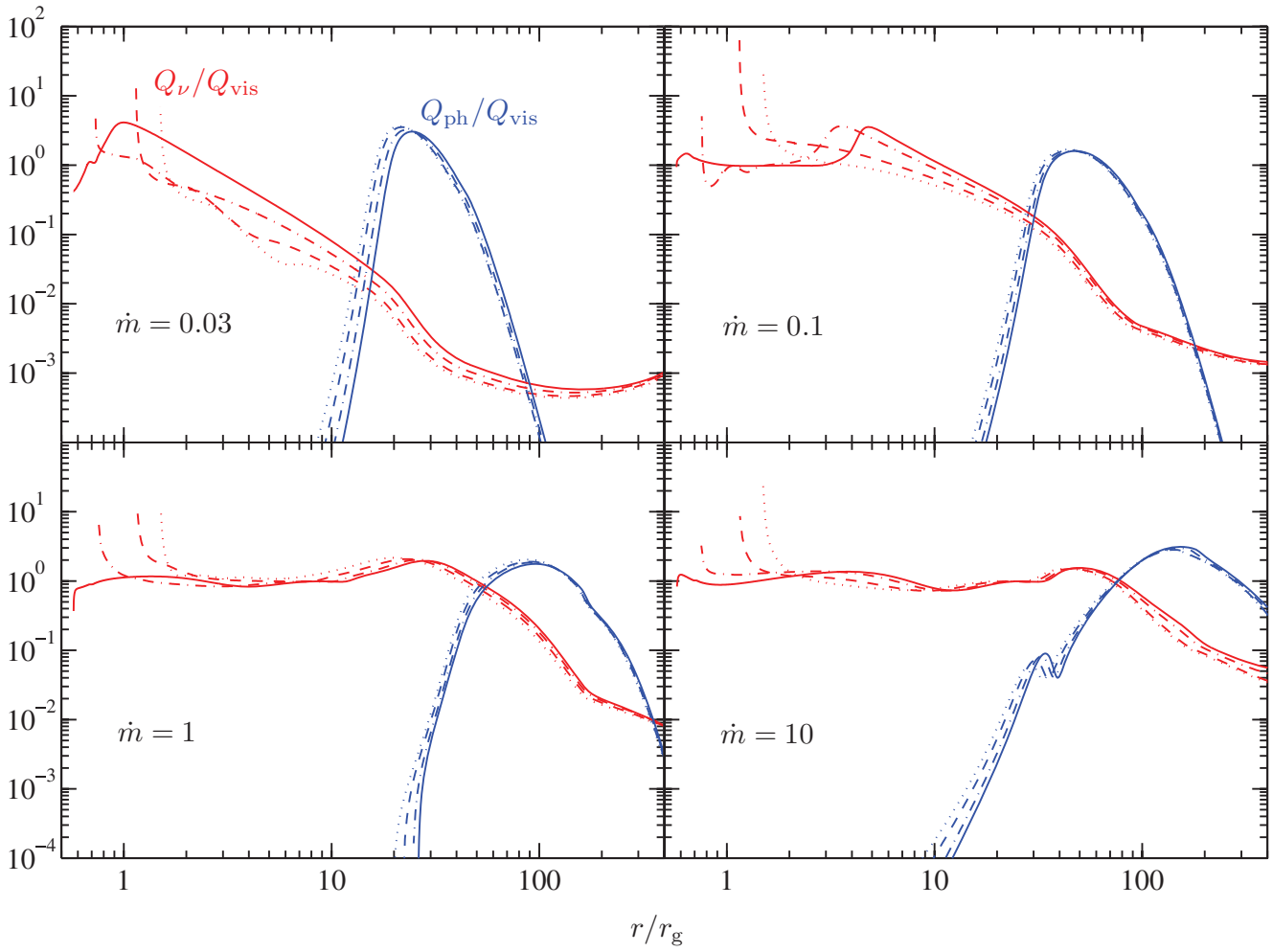

Figure 3. (Continued)

Table 1
Power of NDAFs

a_*	$\dot{M}$ ($M_\odot$ s^{-1})	L_ν (erg s^{-1})	$L_{\nu\bar{\nu}}$ (erg s^{-1})	$L_{\nu\bar{\nu}}/L_\nu$	$r_{\rm tr}(r_{\rm g})$[a]	$r_{\rm ms}(r_{\rm g})$[b]
0.00	0.03	2.04×10^{50}	1.72×10^{44}	8.43×10^{-7}	$<r_{\rm ms}$	3.000
0.00	0.10	4.58×10^{51}	9.11×10^{47}	1.99×10^{-4}	$<r_{\rm ms}$	3.000
0.00	1.00	1.00×10^{53}	8.82×10^{50}	8.82×10^{-3}	$<r_{\rm ms}$	3.000
0.00	10.00	7.60×10^{53}	2.94×10^{52}	3.87×10^{-2}	5.102	3.000
0.50	0.03	6.09×10^{50}	4.91×10^{45}	8.06×10^{-6}	$<r_{\rm ms}$	2.117
0.50	0.10	1.15×10^{52}	9.47×10^{48}	8.23×10^{-4}	$<r_{\rm ms}$	2.117
0.50	1.00	1.52×10^{53}	2.61×10^{51}	1.72×10^{-2}	$<r_{\rm ms}$	2.117
0.50	10.00	1.20×10^{54}	3.17×10^{52}	2.64×10^{-2}	6.095	2.117
0.90	0.03	3.29×10^{51}	3.08×10^{47}	9.36×10^{-5}	$<r_{\rm ms}$	1.160
0.90	0.10	3.45×10^{52}	1.79×10^{50}	5.19×10^{-3}	$<r_{\rm ms}$	1.160
0.90	1.00	3.04×10^{53}	1.76×10^{52}	5.79×10^{-2}	$<r_{\rm ms}$	1.160
0.90	10.00	3.10×10^{54}	3.73×10^{52}	1.20×10^{-2}	7.078	1.160
0.99	0.03	3.11×10^{52}	8.74×10^{49}	2.81×10^{-3}	$<r_{\rm ms}$	0.727
0.99	0.10	7.18×10^{52}	9.30×10^{50}	1.30×10^{-2}	$<r_{\rm ms}$	0.727
0.99	1.00	6.92×10^{53}	5.08×10^{52}	7.34×10^{-2}	1.473	0.727
0.99	10.00	6.38×10^{54}	4.19×10^{52}	6.57×10^{-3}	7.600	0.727

Notes.
[a] $r_{\rm tr}$ is the neutrino trapping radius. $r_{\rm g} = 2M$ is the Schwarzschild radius.
[b] $r_{\rm ms}$ is the radius of the marginally stable orbit.

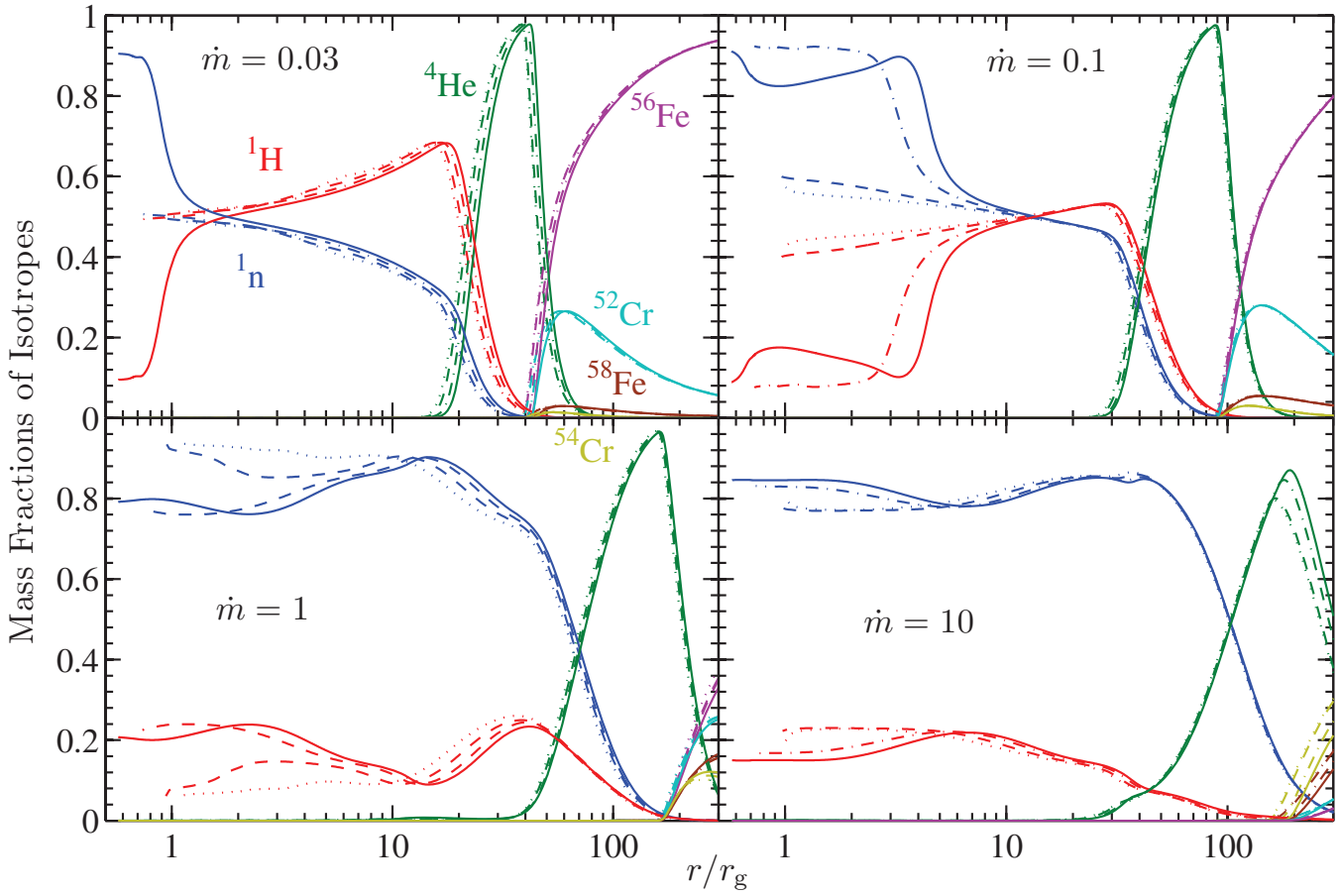

Figure 4. Radial distributions of the mass fraction of seven major nucleons, ^{1}n, ^{1}H, ^{4}He, ^{52}Cr, ^{54}Cr, ^{56}Fe, and ^{58}Fe. The meanings of different line styles are same as in Figures 1, 2, and 3.

(A color version of this figure is available in the online journal.)

where the negative value of $r_{\rm tr}$ predicted by Equation (49) means that there is no trapping in the whole disk.

5. CONCLUSIONS AND DISCUSSION

In this paper, we calculated one-dimensional global solutions of NDAFs, taking into account strict Kerr metric, particular neutrino physics, and precise nucleosynthesis processes, and discussed the structure and luminosity of NDAFs. The electron degeneracy has significant effects in NDAFs, and the electron fraction is about 0.46 in the outer region. From the perspective of the mass fraction, free nucleons, ^{4}He, and ^{56}Fe dominate in the inner, middle, and outer regions, respectively. The influence of neutrino trapping on annihilation is important for the superhigh accretion ($M = 10\,M_{\odot}\,{\rm s}^{-1}$) and most of the 16 solutions have an adequate annihilation luminosity for GRBs.

The inner region of NDAFs may be dynamically unstable (e.g., Janiuk et al. 2007; Kawanaka & Kohri 2012). Time-dependent NDAFs should be calculated, replacing the steady solutions to verify the instability of the disk. Time-dependent accretion disks around Kerr black holes have been investigated by Xue et al. (2011), which can act as the basis for the study of a time-dependent NDAF model.

Jet emission is an essential characteristic of GRB events. Some jet emission mechanisms have been discussed in the literature. Using the magnetic extraction of the rotational energy of a spinning black hole (Blandford & Znajek 1977), Di Matteo et al. (2002) and Kawanaka et al. (2012) estimated the Blandford–Znajek luminosity from NDAFs to budget the energy for jets and relevant GRBs. Recently, Yuan & Zhang (2012) presented an alternative magnetohydrodynamic mechanism for the emission of episodic jets, which can also be used to power GRBs. Without a magnetic field, pair creation by neutrino annihilation outside NDAFs (Eichler et al. 1989), in fact, also has the ability to emit jets and it may possess the additional advantage of low baryonic contamination at the jet ejection point. Our work in this paper belongs to this type of pair creation, but we do not explore this problem deeply in order to avoid unnecessary complexity in the calculation of neutrino annihilation. Thus, our further work is to fully relativistically calculate the neutrino annihilation and the neutrino trapping radius, and to obtain the spatial distribution of energy deposition for our disk model as was done in the works of Zalamea & Beloborodov (2011), and, e.g., Birkl et al. (2007), Kovács et al. (2011), and Kovács & Harko (2011). It may also be attractive if we can combine the pair creation with other magnetic mechanisms (e.g., Blandford & Znajek 1977; Yuan & Zhang 2012), which do not seem to be in conflict with each other.

We thank the anonymous referee for instructive comments and helpful suggestions. This work was supported by the National Basic Research Program (973 Program) of China under Grant 2009CB824800, the National Natural Science Foundation of China under grants 11003016, 11073015, 11103015,

11222328, and 11233006, and the Natural Science Foundation of Fujian Province of China under grant 2010J01017.

REFERENCES

Abramowicz, M. A., Chen, X.-M., Granath, M., & Lasota, J.-P. 1996, ApJ, 471, 762
Abramowicz, M. A., Lanza, A., & Percival, M. J. 1997, ApJ, 479, 179
Birkl, R., Aloy, M. A., Janka, H.-T., & Müller, E. 2007, A&A, 463, 51
Blandford, R. D., & Znajek, R. L. 1977, MNRAS, 179, 433
Burrows, A., & Thompson, T. A. 2004, in Stellar Collapse, ed. C. L. Fryer (Dordrecht: Kluwer), 133
Chen, W.-X., & Beloborodov, A. M. 2007, ApJ, 657, 383
Di Matteo, T., Perna, R., & Narayan, R. 2002, ApJ, 579, 706
Eichler, D., Livio, M., Piran, T., & Schramm, D. N. 1989, Natur, 340, 126
Gu, W.-M., Liu, T., & Lu, J.-F. 2006, ApJL, 643, L87
Itoh, N., Adachi, T., Nakagawa, M., Kohyama, Y., & Munakata, H. 1989, ApJ, 339, 354 (erratum 360, 741 [1990])
Itoh, N., Hayashi, H., Nishikawa, A., & Kohyama, Y. 1996, ApJS, 102, 411
Janiuk, A., Yuan, Y., Perna, R., & Di Matteo, T. 2007, ApJ, 664, 1011
Kato, S., Fukue, J., & Mineshige, S. 2008, Black-Hole Accretion Disks: Towards a New Paradigm (Kyoto: Kyoto Univ. Press)
Kawanaka, N., & Kohri, K. 2012, MNRAS, 419, 713
Kawanaka, N., & Mineshige, S. 2007, ApJ, 662, 1156
Kawanaka, N., Piran, T., & Krolik, J. H. 2013, ApJ, 766, 31
Kohri, K., & Mineshige, S. 2002, ApJ, 577, 311
Kohri, K., Narayan, R., & Piran, T. 2005, ApJ, 629, 341
Kovács, Z., Cheng, K. S., & Harko, T. 2011, MNRAS, 411, 1503
Kovács, Z., & Harko, T. 2011, MNRAS, 417, 2330
Lattimer, J. M., & Swesty, D. F. 1991, NuPhA, 535, 331
Lazzati, D., Campana, S., & Ghisellini, G. 1999, MNRAS, 304, L31
Lee, W. H., Ramirez-Ruiz, E., & Page, D. 2005, ApJ, 632, 421
Lei, W. H., Wang, D. X., Zhang, L., et al. 2009, ApJ, 700, 1970
Li, A., & Liu, T. 2013, A&A, 555, A129
Liu, T., Gu, W.-M., Dai, Z.-G., & Lu, J.-F. 2010a, ApJ, 709, 851
Liu, T., Gu, W.-M., Xue, L., & Lu, J.-F. 2007, ApJ, 661, 1025
Liu, T., Gu, W.-M., Xue, L., & Lu, J.-F. 2012a, Ap&SS, 337, 711
Liu, T., Gu, W.-M., Xue, L., Weng, S.-S., & Lu, J.-F. 2008, ApJ, 676, 545
Liu, T., Liang, E.-W., Gu, W.-M., et al. 2010b, A&A, 516, A16
Liu, T., Liang, E.-W., Gu, W.-M., et al. 2012b, ApJ, 760, 63
Liu, T., Xue, L., Gu, W.-M., & Lu, J.-F. 2013, ApJ, 762, 102
Matsumoto, R., Kato, S., Fukue, J., & Okazaki, A. T. 1984, PASJ, 36, 71
Mihalas, D., & Weibel Mihalas, B. 1984, Foundations of Radiation Hydrodynamics (New York: Oxford Univ. Press)
Nagakura, H. 2013, ApJ, 764, 139
Nagakura, H., Ito, H., Kiuchi, K., & Yamada, S. 2011, ApJ, 731, 80
Narayan, R., Piran, T., & Kumar, P. 2001, ApJ, 557, 949
Ohsuga, K., Mineshige, S., Mori, M., & Umemura, M. 2002, ApJ, 574, 315
Paczyński, B., & Wiita, P. J. 1980, A&A, 88, 23
Pan, Z., & Yuan, Y.-F. 2012a, ApJ, 759, 82
Pan, Z., & Yuan, Y.-F. 2012b, PhRvD, 85, 064004
Popham, R., Woosley, S. E., & Fryer, C. 1999, ApJ, 518, 356
Romero, G. E., Reynoso, M. M., & Christiansen, H. R. 2010, A&A, 524, A4
Rosswog, S., Ramirez-Ruiz, E., & Davies, M. B. 2003, MNRAS, 345, 1077
Ruffert, M., Janka, H.-T., Takahashi, K., & Schäfer, G. 1997, A&A, 319, 122
Sądowski, A. 2009, ApJS, 183, 171
Seitenzahl, I. R., Timmes, F. X., Marin-Laflèche, A., et al. 2008, ApJL, 685, L129
Sun, M.-Y., Liu, T., Gu, W.-M., & Lu, J.-F. 2012, ApJ, 752, 31
Xue, L., Sądowski, A., Abramowicz, M. A., & Lu, J.-F. 2011, ApJS, 195, 7
Yakovlev, D. G., Kaminker, A. D., Gnedin, O. Y., & Haensel, P. 2001, PhR, 354, 1
Yuan, F., & Zhang, B. 2012, ApJ, 757, 56
Yuan, Y.-F. 2005, PhRvD, 72, 013007
Zalamea, I., & Beloborodov, A. M. 2011, MNRAS, 410, 2302
Zhang, B. 2011, CRPhy, 12, 206